Enhanced Photocatalytic H2 Evolution Performance of the Type-II FeTPPCl/Porous g-C3N4 Heterojunction: Experimental and DFT Studies

Journal:	*ACS Applied Materials & Interfaces*
Manuscript ID	am-2023-01683g.R1
Manuscript Type:	Article
Date Submitted by the Author:	25-Feb-2023
Complete List of Authors:	Humayun, Muhammad; Huazhong University of Science and Technology, School of Optical and Electronics Information Ullah, Habib; Environment and Sustainability Institute , Renewable Energy Hu, Chao; Huazhong University of Science and Technology Tian, Mi; University of Bath, Chemical Engineering Pi, Wenbo; Huazhong University of Science and Technology Zhang, Yi; Wuhan Institute of Technology, School of Chemical Engineering and Pharmacy Luo, Wei; Huazhong University of Science and Technology, Wang, Chundong; Huazhong University of Science and Technology, School of Optical and Electronic Information

Enhanced Photocatalytic H_2 Evolution Performance of the Type-II FeTPPCl/Porous g-C_3N_4 Heterojunction: Experimental and DFT Studies

Muhammad Humayun[†], Habib Ullah[‡,ǂ], Chao Hu[†,ǁ], Mi Tian[ǂ], Wenbo Pi[†], Yi Zhang[ǁ], Wei Luo[†,*] and Chundong Wang[†,*]

[†]School of Optical and Electronic Information, Wuhan National Laboratory for Optoelectronics, Engineering Research Center for Functional Ceramics of the Ministry of Education, Huazhong University of Science and Technology, Wuhan 430074, People's Republic of China

[‡]Department of Renewable Energy, Faculty of Environment, Science and Economy, University of Exeter, Penryn Campus, Cornwall TR10 9FE, United Kingdom

[ǂ]Department of Engineering, Faculty of Environment, Science and Economy University of Exeter, EX4 4QF, United Kingdom

[ǁ]School of Chemical Engineering and Pharmacy, Wuhan Institute of Technology, Wuhan, 430073, China

*Authors to whom correspondence should be addressed: luowei@mail.hust.edu.cn (W. Luo); apcdwang@hust.edu.cn (C.D. Wang)

KEYWORDS: Porous g-C_3N_4; Density functional theory; Chemical exfoliation; FeTPPCl porphyrin; Water reduction; Type-II heterostructure.

ABSTRACT: It is of great significance to improve the photocatalytic performance of g-C_3N_4 by promoting its surface-active sites and engineering more suitable and stable redox couples. Herein, first of all, we fabricated porous g-C_3N_4 (PCN) via the sulfuric acid-assisted chemical exfoliation method. Then, we modified the porous g-C_3N_4 with Iron(III) meso-tetraphenylporphine chloride (FeTPPCl) porphyrin via the wet-chemical method. The as-fabricated FeTPPCl-PCN composite revealed exceptional performance for photocatalytic water reduction by evolving 253.36 and 8301 μmolg^{-1} of H_2 after visible and UV-visible irradiation for 4 h, respectively. The performance of the FeTPPCl-PCN composite is ~2.45 and 4.75-fold improved compared to that of the pristine PCN photocatalyst under the same experimental conditions. The calculated quantum efficiencies of the FeTPPCl-PCN composite for H_2 evolution at 365 and 420 nm wavelengths are 4.81 and 2.68%, respectively. This exceptional H_2 evolution performance is because of improved surface-active sites due to porous architecture and remarkably improved charge carrier separation via the well-aligned type-II band heterostructure. Besides, we also reported the correct theoretical model of our catalyst through density functional theory (DFT) simulations. It is found that the hydrogen evolution reaction (HER) activity of FeTPPCl-PCN arises from the electron transfer from PCN via Cl atom(s) to Fe of the FeTPPCl, which forms a strong electrostatic interaction, leading to a decreased local work function on the surface of the catalyst. We suggest that the resultant composite would be a perfect model for the design and fabrication of high-efficiency heterostructure photocatalysts for energy applications.

1. INTRODUCTION

Owing to the rapid consumption of fossil fuels energy reservoirs and subsequent environmental contamination, hydrogen production via solar water splitting with the aid of semiconductor photocatalytic materials received tremendous attention.[1-3] Hydrogen is recognized as a clean and green form of energy carrier alternative to fossil fuels energy because of its abundance, zero-emission, virtuous combustibility, and high specific calorific value (i.e., 120-142 Megajoules).[4] From environmentally friendly and economic perspectives, earth-abundant, highly efficient, nontoxic, and stable photocatalysts capable of light harvesting are required. In this regard, prodigious efforts have been devoted to highly efficient H_2 generation by utilizing a variety of semiconductor photocatalytic materials including metal oxides, metal carbides, metal nitrides, noble metal, and non-noble metal-based photocatalysts.[5]

As a benchmark photocatalyst, anatase TiO_2 is widely employed for solar H_2 production through water-splitting reactions owing to its low cost, excellent stability, and exceptional efficiency under UV-light illumination.[6,7] Yet, the benchmark TiO_2 still suffers from several drawbacks including

the sluggish proton reduction kinetics, limited solar energy consumption, and rapid recombination rate of photoinduced charge carriers.[8,9] Thus, it is of utmost interest to design and develop high-performance semiconductor photocatalytic materials for practical applications. In fact, the photocatalytic water splitting process requires appropriate semiconductor photocatalysts with their conduction band bottom value negative than that of the proton reduction potential (i.e., 0 V) and their valence band top value positive than that of the water oxidation potential (i.e., 1.23 V).[10,11] Usually, in the majority of the designed photocatalysts, the rapid charge carrier's recombination rate results in low H_2 generation and solar-to-fuel conversion efficiency. Further, the photoinduced holes self-oxide the photocatalysts (photo-corrosion). In addition, during photocatalytic water splitting reaction, the H_2 generation safety should also be well-organized because the H_2 and O_2 mixture are explosive and explode when the H_2 concentration exceeds the explosion limit (i.e., 4-75%). That's why some sacrificial agents like methanol, triethanolamine, etc., are added to consume the photoinduced holes, thereby avoiding the safety accident of explosion, prolonging the charge carrier's lifetime, and improving the H_2 generation rate.[9,12-14]

With the wide-ranging implementation in mind, substantial efforts have been devoted to developing narrow band gap semiconducting photocatalytic materials based on earth-abundant elements. Recently, graphitic carbon nitride (g-C_3N_4) received marvelous attention in photocatalytic solar energy conversion due to its exceptional optical and electronic structure, high chemical and thermal stability, and polymeric nature.[15] Due to the presence of aromatic C−N heterocyclic rings, g-C_3N_4 is thermally stable up to 600 °C in air atmosphere. Further, due to the existence of strong van der Waal's forces in its layers, g-C_3N_4 exhibit high chemical stability in various solvents including H_2O, diethyl ether, toluene, alcohols, glacial acetic acid, tetra-hydrofuran, N, N-dimethyl-formamide, and 0.1 M NaOH.[16] Generally, polymeric g-C_3N_4 is mainly composed of carbon (C) and nitrogen (N) elements, and some impurity hydrogen (H), linked through the tris-triazine patterns, and it can be directly synthesized via the condensation polymerization of a variety of inexpensive N-rich precursor materials such as melamine, urea, cyanamide, thiourea, dicyandiamide, and ammonium thiocyanate. Until now, g-C_3N_4 is widely utilized in photocatalysis for several applications, such as H_2 generation, water decontamination, and CO_2 conversion.[17-21] Yet, the performance of g-C_3N_4 is inadequate for potential photocatalysis owing to its limited solar energy harvesting capability, small surface area, and rapid recombination rate of charges.[22] Since the photocatalytic performance of semiconducting photocatalytic materials is directly linked to these factors, thus, it is essential to modify the electronic and structural features of g-C_3N_4 so as to promote its photoactivity.

Numerous strategies including surface morphology alteration, elemental doping, defect engineering, and heterostructures formation have been utilized to improve the photophysics and photochemistry of g-C_3N_4 for better product yield.[16] Among different strategies, the chemical exfoliation of bulk g-C_3N_4 into a few layers of g-C_3N_4 for enhanced photoactivities received tremendous attention. For instance, Papailias et al.[23] prepared a few layered g-C_3N_4 from bulk material via the chemical exfoliation method that revealed exceptional visible light activity for NOx removal. In another work by Tong et al.[24] the g-C_3N_4 nanosheets obtained from bulk via the chemical exfoliation revealed superior visible light catalytic performance for hydrogen evolution. This exceptional performance was accredited to the improved surface-active sites.

Besides morphological changes, the modification of g-C_3N_4 with porphyrins (heterocyclic macrocycles) received marvelous attention because of their π-π interaction. Due to their semiconducting nature, broad absorption band, plentiful conjugate π bonds, and excellent charge mobility, porphyrins are utilized as promising photocatalysts in photocatalysis for various applications. The efficient charge separation and transfer in such types of composite systems are highly decisive to achieve exceptional photocatalytic performance.[25] For instance, Zhang et al.[26] reported the g-C_3N_4-C_x/FeTCPP composite photocatalysts that revealed enhanced activity for CO_2 conversion to CO and H_2. Likewise, Chen et al.[27] reported the synthesis of CuTCPP/g-C_3N_4 composite system that revealed exceptional visible light catalytic activity for phenol degradation. In our recent report,[28] the fabricated Au-porphyrin/g-C_3N_4 Z-scheme composite system revealed excellent H_2 evolution under UV–visible irradiation. To the best of our knowledge, there is no previous report on the fabrication of Iron(III) meso-tetraphenylporphine chloride/g-C_3N_4 composite system, especially for photocatalytic water splitting to evolve H_2.

Herein, first of all, we fabricated a few layers of porous g-C_3N_4 via the chemical exfoliation method. Then, we modified the as-fabricated porous g-C_3N_4 (PCN) with Iron(III) meso-tetraphenylporphine chloride (FeTPPCl) porphyrin via the wet-chemical method. The performance of the resultant PCN-FeTPPCl photocatalyst was evaluated by water reduction to evolve H_2 under visible and UV-visible illumination. The PCN-FeTPPCl composite revealed exceptional photocatalytic performance by producing 253.36 and 8301 $\mu molg^{-1}$ of H_2 under visible and UV-visible illumination, respectively, which is ~2.45 and 4.75-fold higher than that of the pristine PCN. This exceptional performance for H_2 generation is accredited to the surface exposed abundant active sites due to porous structure and to the significantly promoted charge carrier's separation and transfer via the well-aligned type-II band heterostructure. In order to check and confirm the performance of our reported catalyst, density functional theory (DFT) simulations of PCN-FeTPPCl were performed. We built two different types of models for the PCN-FeTPPCl, and based on the excellent performance and correlation with experimental data; the exact model of the catalyst. A strong electrostatic interaction of -1.51 eV between PCN and FeTPPCl validates the stability and feasibility of PCN-FeTPPCl, where the electronic cloud density has moved to FeTPPCl (surface became more electronegative) and can easily cause water reduction. Finally, we suggest that this work will help in the development of high-efficiency heterostructure photocatalysts for solar energy conversion and storage.

2. EXPERIMENTAL SECTION

2.1. Materials. Melamine ($C_3H_6N_6$; MW 126.12), Sulfuric acid (H_2SO_4; MW 98.08), Iron(III) meso-tetraphenylporphine chloride ($C_{44}H_{28}ClFeN_4$; MW 704.02) represented as FeTPPCl, Acetylacetone ($C_5H_8O_2$; MW 100.12) and Absolute ethanol (C_2H_5OH; 46.07) were obtained from Sinopharm Chemical

Reagent Co., Ltd. Shanghai China. De-ionized water was used throughout the experiments.

2.2. Synthesis of Bulk g-C_3N_4. The bulk g-C_3N_4 was obtained directly via the condensation polymerization of melamine precursor. About 40g of bulk g-C_3N_4 was obtained via the direct calcination of melamine precursor at 550 °C for 2h (rise in temp: 5 °C min^{-1}). The as-obtained yellow product of bulk g-C_3N_4 was ground into fine powder.

2.3. Synthesis of Porous g-C_3N_4 Nanosheets. To obtain a few layers of porous g-C_3N_4 nanosheets, about 40g of the bulk g-C_3N_4 was dispersed in 400 mL of concentrated H_2SO_4 (contained in a 1000 mL beaker) under ultrasonication at room temperature. After ultrasonication for 30 min, 100 mL of de-ionized H_2O was added to the dispersion. An exothermic reaction took place and the whole bulk g-C_3N_4 suddenly disappeared and a transparent yellow solution was obtained. After dilution with an excess amount of deionized water, a sponge-like white colony appeared (Supporting Information Figure S1a). While keeping the solution under static conditions for the whole night, the sponge colony settled down at the bottom of the beaker and the supernatant solvent was thrown away. The precipitate was centrifuged and washed with de-ionized H_2O and ethanol in turn. Finally dried in a vacuum oven at 85 °C, and then calcined at 550 °C for 2h. The as-obtained product was labeled as PCN.

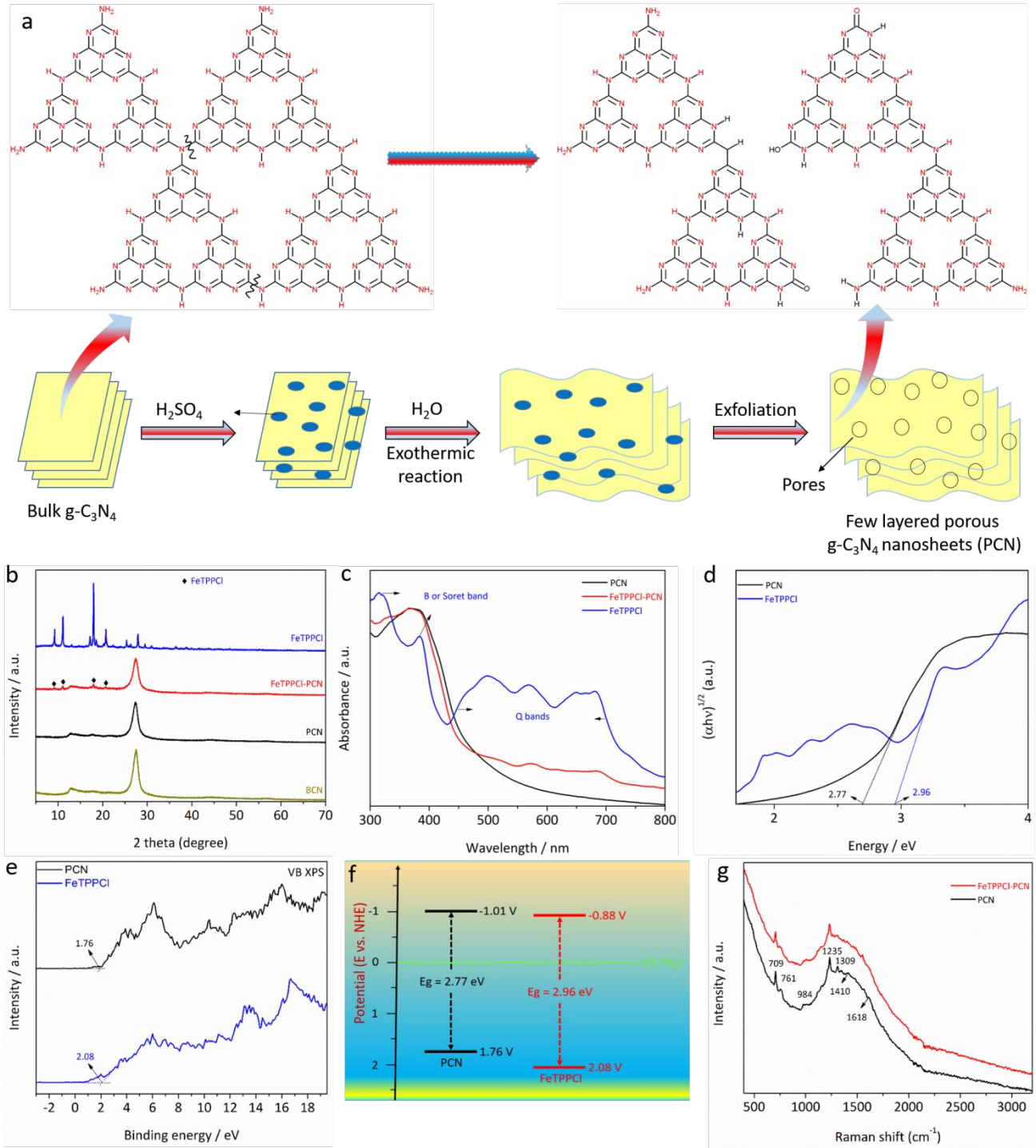

Figure 1 (a) Scheme for the transformation of bulk g-C_3N_4 into a few layered porous g-C_3N_4 nanosheets via the chemical exfoliation method. (b) XRD patterns, (c) UV-visible absorption spectra, (d) Predicted band gaps via Tauc plots of $(\alpha h\nu)^{1/2}$ vs. photon energy, (e) Valence band XPS spectra, (f) Energy bands diagram vs. the NHE, and (g) Raman spectra of the photocatalysts.

2.4. Synthesis of FeTPPCl/PCN composite. To fabricate FeTPPCl/PCN composite, $1*10^{-1}$ M solution of FeTPPCl was prepared in 10 mL of acetylacetone. Then, 1g of the PCN powder was dispersed in the above solution and stirred for 24h. The dispersion was centrifuged thoroughly, washed with acetylacetone, and then dried in a vacuum oven at 85 ^{o}C.

2.5. Characterizations. The X-ray diffraction pattern of the photocatalysts was evaluated with x′pert3 PANalytical powder XRD spectrometer (Netherlands) with Cu Kα source. The UV–vis spectrophotometer (SolidSpec-3700; Shimadzu, Japan) was utilized for the measurement of absorption spectra. The catalyst morphology and energy dispersive spectroscopy (EDS) X-ray analysis was done with ZEISS-G300 (Germany) scanning electron microscope (SEM). The Tecnai FEI-G2-F30-(USA) transmission electron microscope (TEM) was employed for collecting micro images of the catalysts. An X-ray photoelectron spectrometer (ESCALAB-250XI; USA) (XPS) was used for analyzing the chemical composition of the catalysts. The VERTEX-70 Bruker Fourier-transform-infrared spectrometer (FTIR, Germany) was employed for surface-functional groups analysis of the catalysts. A LabRAM-HR800 (Horiba-Jobin Yvon; (France)) was used for Raman spectroscopy analysis of the catalysts. The FP-6500 (Japan) fluorescence spectrometer was used for the detection of PL spectra of the catalysts. An instrument connected to the lock-in-amplifier (SR830, USA) and light chopper (SR540, USA) was used for surface-photovoltage (SPV) spectra measurement. The Brunauer–Emmett–Teller (BET) surface area and pore size distribution curves of the photocatalysts were obtained with Mike-3Flex (USA) using N_2 adsorption/desorption technique. A Brooker-A300 instrument was employed for electron-paramagnetic resonance (EPR) analysis. The fluorescence decay spectra were measured with EDINBURGH-FLS-980 (UK) instrument. A Perkin Elmer TGA-8000 (USA) was employed for thermogravimetric analysis in the range of 30–780 °C (air environment). The photoelectrochemical (PEC) and electrochemical measurements were performed with CHI-760E instrument (Shanghai, China) using the Ag/AgCl as a reference electrode.

2.6. Photocatalytic Hydrogen Production. The CEAULIGHT-CEL-SPH2N-D9 (Beijing; China) instrument was employed for water-splitting experiments to generate hydrogen with the assistance of methanol (sacrificial agent). 50 mg of the catalyst was dispersed in the methanol-water mixture (1:5 by vol) under continuous stirring. The system was thoroughly degreased for 30 min to remove bubbles. Then, the photocatalytic experiments were performed under visible and UV–visible illumination using a Perfect-light 300 W Xenon lamp (Beijing; China). The hydrogen generated via the photocatalytic reaction was detected with the online CEAULIGH GC-7920 gas chromatograph (N_2 as the carrier gas) connected to the TCD detector.

3. RESULTS AND DISCUSSION

3.1. Fabrication, Structural Morphology and Chemical Composition. The fabrication of a few layers of porous g-C_3N_4 nanosheets (PCN) was done by the stepwise chemical exfoliation of the bulk g-C_3N_4 (BCN) as depicted in Figure 1a.

The X-ray diffraction (XRD) pattern of the BCN, PCN, FeTPPCl-PCN composite, and FeTPPCl are displayed in Figure 1b. As obvious, the bulk CN sample contains two distinctive diffraction peaks at 13.1° and 27.5°. The peak at 13.1° with an interplanar distance of 0.67 nm corresponds to the in-plane structural packing motif of the tri-s-triazine rings, which usually directs the (100) plane. The peak at 27.5° with an interplanar distance of 0.32 nm corresponds to the inter-layer stacking interaction of aromatic rings, which usually directs the (002) plane. After chemical and thermal treatment, the peak intensity of (100) and (002) planes of the PCN sample remarkably decreased demonstrating a reduction in interplanar distance and the aligned layers. This reduction in peak intensity confirms the delamination and increase in layers disorder.[23] Worth noting, some major characteristic peaks of the FeTPPCl component are detected in the XRD pattern of the FeTPPCl-PCN composite, directing the presence of a strong chemical interaction between the two-component systems. In order to evaluate the optical and electronic band structure of the photocatalysts, UV-visible absorption spectra, and the valence band X-ray photoelectron spectra were recorded. According to our previous report,[29] the BCN revealed an energy band gap of 2.7 eV, comparable to the threshold energy absorption wavelength of 459 nm. As clear from Figure 1c, the threshold energy absorption wavelength of PCN is 448 nm, which confirms an increase in band gap via the chemical exfoliation process. Further, the threshold absorption wavelength of FeTPPCl and FeTPPCl-PCN photocatalysts is located at 419 and 441 nm, respectively. Worth noting, the bare FeTPPCl exhibit two types of bands, the B or Soret band, and Q-bands. The strong absorption Soret band at approximately 384 nm is ascribed to the S0 to S2 transition, while the less intense absorption Q bands in the range of 450 to 720 nm are ascribed to the S0 to S1 transition. The metallated porphyrins usually possess the fully resolved split Soret band which is caused by the mixing of Soret and Q-states. In FeTPPCl, the Q band is split due to the vibrational excitations. Therefore, two bands are produced due to the transition from the ground state to two vibrational states of the excited state [Q(0,0) and Q(1,0)]. The presence of NH protons breaks the symmetry and each of the above-mentioned band further split into two bands. The X and Y components no longer degenerate and hence we see four Q-bands Qx(0,0), Qy(0,0), Qx(1,0) and Qy(1,0). Thus, the strong electronic transitions associated with the UV region are designated as the Soret or B-resonance and the forbidden or weak transitions in the visible light region are designated as the Q-bands or Q-transitions.[30-32] As obvious, the Q-bands of FeTPPCl catalyst also appeared in the FeTPPCl-PCN composite, confirming the existence of strong chemical interaction between the well-aligned two components system. In addition, the absorption wavelength of FeTPPCl-PCN composite is slightly blue-shifted toward the FeTPPCl catalyst. The energy band gaps of the PCN (i.e., 2.77 eV), and FeTPPCl (i.e., 2.96 eV) catalysts were predicted from the Tauc plots as revealed in Figure 1d.

Valence band XPS spectra were measured for the valence and conduction bands maxima values of the PCN and FeTPPCl catalysts. As clear from Figure 1e, the valence band maxima

values of PCN and FeTPPCl catalysts are predicted to be 1.76 and 2.08 eV, respectively. Hence, the conduction band maxima values of the PCN (-1.01 V) and FeTPPCl (-0.88 V) catalysts were predicted from the experimentally observed energy band gaps and valence band maxima values, according to the equation reported in literature.[33] For better understanding, the band gap values and the conduction and valence band potentials of the photocatalysts vs. the NHE are displayed in Figure 1f. To further probe the crystal structure and variation in lattice symmetry of the PCN and FeTPPCl-PCN photocatalysts, Raman spectra were analyzed as depicted in Figure 1g. As clear, the Raman peaks in PCN photocatalyst are the characteristics of g-C_3N_4 motif. The peak at 709 cm^{-1} corresponds to the vibrational mode of the s-triazine patterns. The peaks at 761, 984, and 1235 cm^{-1} are ascribed to the stretching vibrational mode of the aromatic heterocycles in melem. The peaks centering at 1309 and 1618 cm^{-1} correspond to the D-band and G-band, respectively, confirming the g-C_3N_4 structure. Worth noting, the Raman spectrum of FeTPPCl-PCN photocatalyst reveals similar characteristic peaks, signifying that the introduction of FeTPPCl not damaged the skeleton network of PCN. Nevertheless, a slight blue shift in the Raman bands of FeTPPCl-PCN with respect to the PCN photocatalyst can be observed, which might be due to the strong chemical interaction between both of the components.[29]

To investigate the morphology of the photocatalysts, SEM analysis was done. As revealed in the Supporting Information Figure S1b, the bulk CN shows a nonporous architecture of the aggregated flakes. The chemically exfoliated PCN photocatalyst (Supporting Information, Figure S1c) reveals a 3D sponge-like framework with a unified porous structure, which resulted from the acid intercalation of bulk CN. Further, the nanosheet layers become thinner after the acid treatment and annealing. The SEM micrograph of FeTPPCl-PCN composite (Supporting Information, Figure S1d) reveals the presence of FeTPPCl nanoparticles anchored onto the surface of PCN photocatalyst. A transmission electron microscope was used to further investigate the microstructure of the photocatalysts. The TEM and selected area HRTEM images of the PCN photocatalysts are depicted in Figure 2a, b. The TEM images of PCN clearly reveal thin layers of nanosheets with uniformly distributed nanometric-size pores. The TEM image of FeTPPCl (Supporting Information Figure S2a) clearly reveals the aggregation of a large number of molecule particles. The average size of the aggregated FeTPPCl molecule particles is approximately in the range of 80-200 nm. In the selected area HRTEM image of FeTPPCl (Supporting Information Figure S2b), no lattice fringes can be observed confirming its macrocyclic molecular nature. The TEM image of FeTPPCl-PCN composite (Figure 2c) clearly reveals the chemically anchored FeTPPCl nanoparticles on the surface of PCN. Further, the selected area HRTEM images of the FeTPPCl-PCN composite (Figure 2d-f) reveal distinct boundaries of single components.

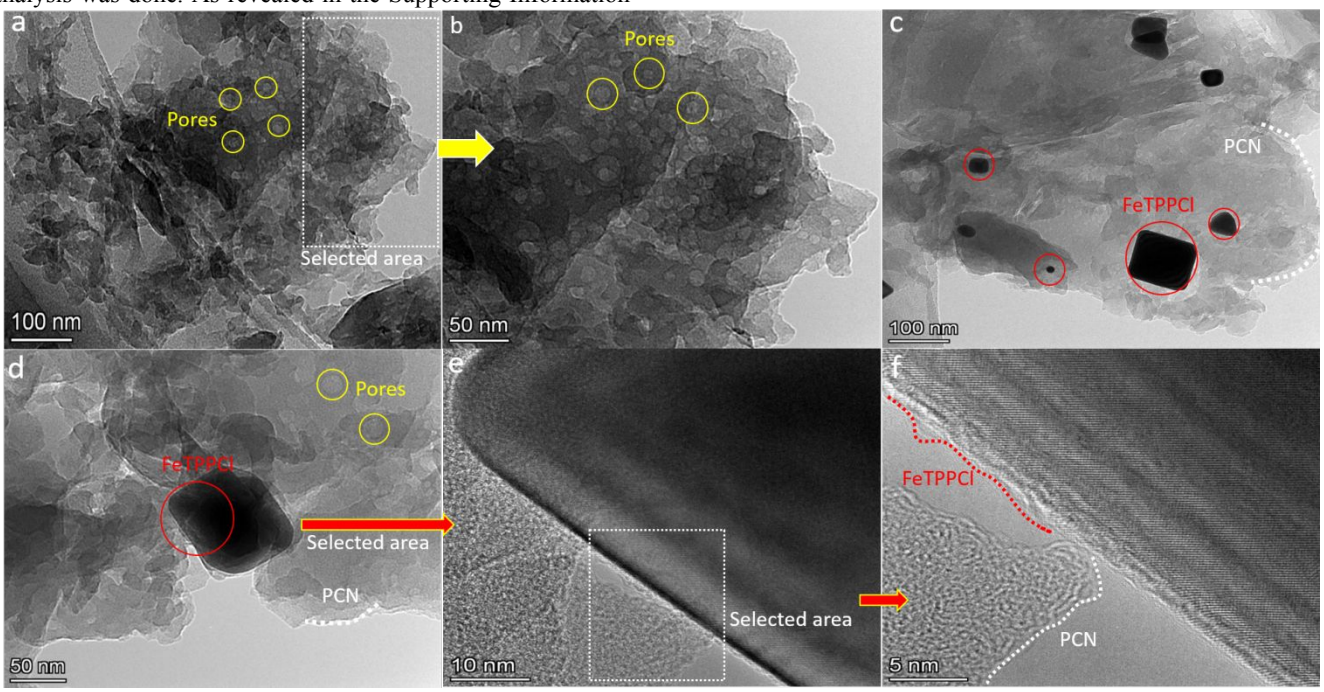

Figure 2 (a) TEM micrograph, and (b) HRTEM micrograph of PCN. (c) TEM micrograph and (d-f) HRTEM micrographs of the FeTPPCl-PCN composite.

To investigate the porous structure of the photocatalysts, N_2 sorption analysis was performed. The N_2 adsorption/desorption isotherm curve of bulk CN is provided in the Supporting Information Figure S2c, while that of the PCN, FeTPPCl-PCN, and FeTPPCl photocatalysts are revealed in Figure 3a. As obvious, all the photocatalysts reveal type IV isotherm curves according to the classification by Brunauer, Deming, Deming, and Teller (BDDT). This confirms the presence of mesopores in the as-fabricated photocatalysts. The shapes of the hysteresis loops for all photocatalysts are of type H3, which is resulted from the slit-like mesopores generated due to the sheet-like particles aggregation.[34,35] The observed BET specific surface area of the bulk CN is 3.17 m^2 g^{-1} (Supporting Information Figure S2c inset), while the surface areas of PCN and FeTPPCl photocatalysts are 24.72 m^2 g^{-1} and 7.5 m^2 g^{-1}, respectively as mentioned in the inset of Figure 3a.

As obvious, the BET specific surface area of the FeTPPCl-PCN composite (i.e., 27.4 m^2 g^{-1}) is slightly larger than that of the bare PCN photocatalyst. The BJH pores size distribution curve of bulk CN (Supporting Information Figure S2d) confirmed its pore diameter in the range of 5-150 nm. The BJH pores size distribution curves of the PCN, FeTPPCl-PCN, and FeTPPCl photocatalysts are depicted in Figure 3b. As clear, the small mesopores designated by several peaks of ~20 nm could be accredited to the uniform porosity in PCN and FeTPPCl-PCN photocatalysts. This might be due to the rapid exothermic reaction upon the addition of H_2O to the dispersion of bulk CN in H_2SO_4, which cause delamination of bulk CN. The resultant high specific surface area and the mesoporous structure are expected to provide abundant active sites for catalytic reactions.[36]

To investigate the chemical composition of the PCN and FeTPPCl-PCN photocatalysts, FT-IR spectra were obtained as revealed in Figure 3c, d. The FT-IR spectrum of PCN photocatalyst clearly reveals an apparent peak at 808 cm^{-1}, corresponding to the bending vibration mode of the tri-s-triazine patterns. The characteristic bands in the range of 1236–1635 cm^{-1} are accredited to the C–N heterocycles. The wide band at 3000–3300 cm^{-1} is accredited to the adsorbed OH^- species on the surface and the corresponding amino groups.[37,38] In the case of the FeTPPCl-PCN photocatalyst, the characteristic band at 999 cm^{-1} could be accredited to the Fe-N bond formation. The peak at 3400 cm^{-1} is accredited to the amino groups. The peaks in the range of 1539-1696, and at 1380 cm^{-1} can be accredited to the C=C stretching and the C–N stretching vibration modes, respectively. The broadband corresponding to the N–H vibration mode of PCN at 3000-3300 cm^{-1}, slightly switched to a larger wavenumber demonstrating the probable effect of hydrogen bonding of N–H groups of PCN with the phenyl groups of FeTPPCl. Further, the overlapping of FeTPPCl peak at 808 cm^{-1} with that of the PCN component can be clearly observed. The FT-IR results further clarify the presence of strong chemical interaction between the PCN and FeTPPCl components in the FeTPPCl-PCN composite.

The X-ray photoelectron spectroscopy measurement was done to evaluate the composition and elemental chemical states of the PCN, FeTPPCl, and FeTPPCl-PCN photocatalysts. The survey spectra of PCN, FeTPPCl, and FeTPPCl-PCN photocatalysts (Supporting Information, Figure S3a, b) revealed the corresponding elements of each sample. The C 1s (Supporting Information, Figure S3c) and N 1s (Supporting Information, Figure S3d) XPS spectrum of FeTPPCl photocatalyst reveals binding energy peaks at 284.83 and 398.8 eV, corresponding to the sp^2 hybridized carbon atoms and the Fe–N bonds in metalloporphyrin, respectively. The deconvoluted Fe 2p XPS spectrum of FeTPPCl (Supporting Information, Figure S3e) reveals two peaks at 711.8 and 725.18 eV, corresponding to the Fe $2p_{3/2}$ and Fe $2p_{1/2}$ orbitals of Iron(III) porphyrin, respectively. In addition, the deconvoluted Cl 2p XPS spectrum of FeTPPCl (Supporting Information, Figure S3f) reveals two peaks at binding energy values of 198.48 and 200.13 eV, corresponding to the Cl $2p_{3/2}$ and Cl $2p_{1/2}$ orbitals, respectively.[39] The C 1s spectra of PCN and FeTPPCl-PCN photocatalysts are revealed in Figure 3e. The C 1s spectrum of PCN photocatalyst can be deconvoluted into two peaks corresponding to the sp^2-hybridized C−C (i.e., 284.84 eV) and sp^2-hybridized N−C=N (i.e., 288.08 eV) coordination. Similarly, the C 1s spectrum of FeTPPCl-PCN composite exhibit two peaks at 284.91 and 288.34 eV, respectively, corresponding to the sp^2-hybridized C−C and N−C=N bonds. Worth noting, the increase in binding energy value of the C−C and N−C=N coordination of FeTPPCl-CN led us to know that the electron density of PCN is reduced due to the transfer of electrons from PCN to FeTPPCl.[40] The N 1s spectra of PCN and FeTPPCl-PCN photocatalysts are depicted in Figure 3f. As obvious, the N 1s spectrum of PCN can be deconvoluted into three prominent peaks centering at 398.42, 399.33, and 400.77 eV, corresponding to the sp^2-hybridized C − N=C, N-$(C)_3$, and C − N − H coordination, respectively. After the introduction of FeTPPCl, a slight increase in the binding energies of C − N=C (398.74 eV), N-$(C)_3$ (399.41 eV), and C − N − H (400.81 eV) bonds can also be observed.[10] The Fe 2p spectrum of FeTPPCl-PCN composite (Figure 3g) can be deconvoluted into two major peaks at binding energy values of 710.7 and 724.0 eV, which corresponds to the Fe $2p_{3/2}$ and Fe $2p_{1/2}$ orbitals of Fe^{+3} state of Iron(III) porphyrin in which Fe^{3+} is coordinated with N atoms.[41] The deconvoluted Cl 2p spectrum of FeTPPCl-PCN composite (Figure 3h) exhibits two peaks centering at 197.99 and 199.58 eV, accredited to the Cl $2p_{3/2}$ and Cl $2p_{1/2}$ orbitals, respectively.[42]

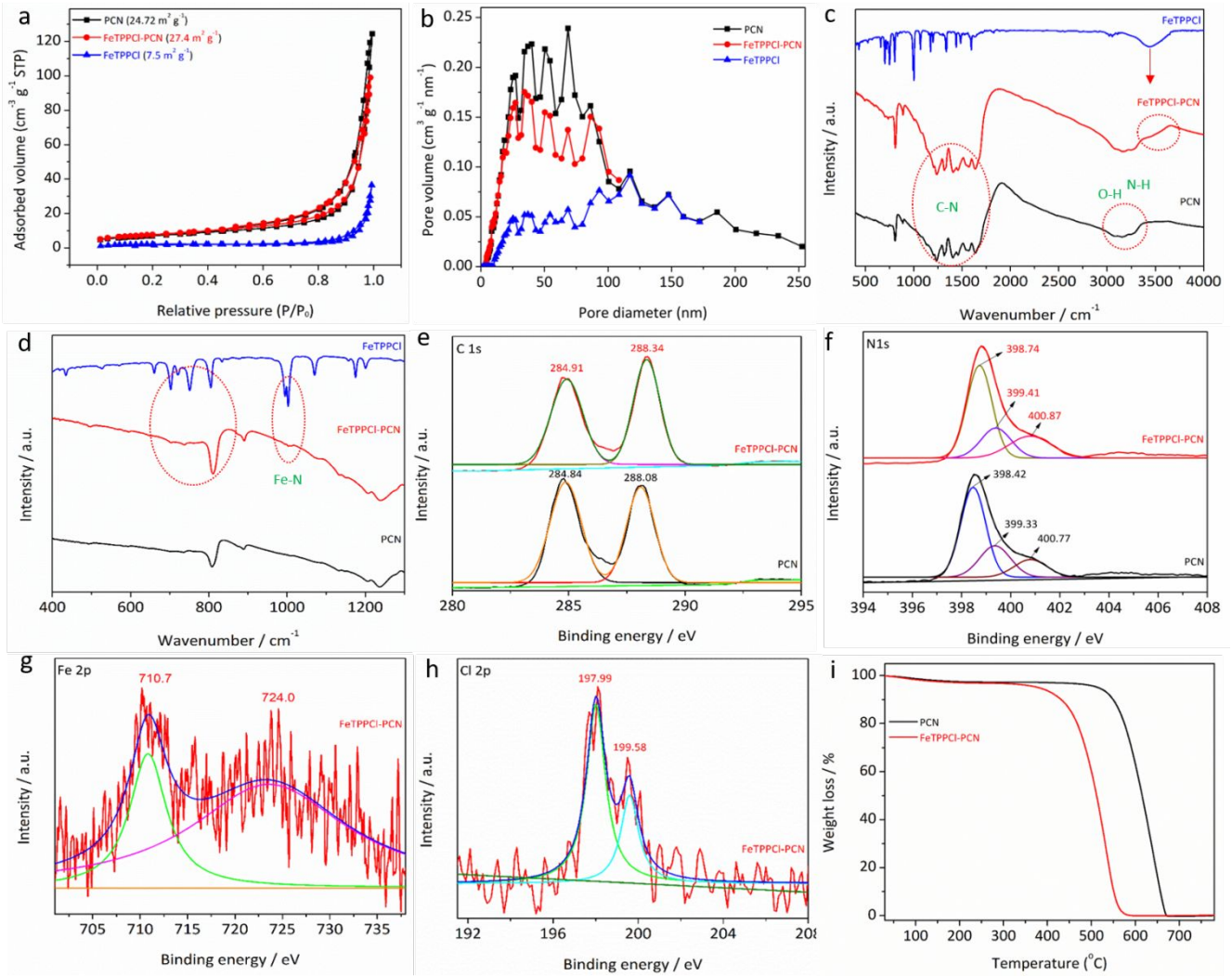

Figure 3 (a) BET N_2 adsorption-desorption isotherm curves, and (b) pore size distribution curves of the PCN, FeTPPCl-PCN, and FeTPPCl photocatalysts. (c, d) FT-IR spectra of PCN, FeTPPCl-PCN, and FeTPPCl photocatalysts. XPS spectra: (e) C 1s, and (f) N 1s, of the PCN and FeTPPCl-PCN photocatalysts. (g) Fe 2p and (h) Cl 2p of FeTPPCl-PCN photocatalyst. (i) Thermo-gravimetric analysis spectra of PCN and FeTPPCl-PCN photocatalysts measured in the range of 30-780 °C.

Thermogravimetric analysis (TGA) was done to investigate the weight loss of the samples after heat treatment in the range of 30-780 °C. The TGA result of PCN (Figure 3i) reveals a rapid weight loss in the range of 600–670 °C, which means the thermal decomposition of PCN starts at 600 °C. Further, the weight loss of FeTPPCl-PCN composite starts at 500 °C. This signifies that the thermal stability of PCN photocatalyst is slightly decreased after incorporation of the FeTPPCl.

3.2. Charge Carriers Separation. To explore photoinduced charge separation and transfer in the as-synthesized photocatalysts, surface photo-voltage (SPV) spectroscopy was employed. SPV spectroscopy is mainly used for the investigation of the surface physical phenomenon occurring in semiconductors in terms of excitation, separation, and transfer of charge carriers. The SPV technique usually detects the charge carrier's separation in the form of a signal. Enhancement in the charge carrier's separation gives rise to a strong SPV signal.[43,44] As clear from Figure 4a, the SPV signal of FeTPPCl-PCN composite is remarkably enhanced compared to that of the bare PCN and FeTPPCl photocatalysts, suggesting superior charge separation and transfer in the as-fabricated composite. To corroborate the SPV results, photoluminescence (PL) spectroscopy was further used to explore the photophysics of photoinduced charge carriers in the PCN, FeTPPCl and FeTPPCl-PCN photocatalysts. Usually, from PL technique, we can get information regarding the surface defects, vacancies, and surface recombination of photoinduced charges.[38,45] As clear from Figure 4b, the FeTPPCl and PCN photocatalysts exhibit strong PL signal, directing rapid charge carrier recombination. However, a significant quenching in the PL signal is observed for the FeTPPCl-PCN composite in comparison to the PCN and FeTPPCl photocatalysts. This result led us to know that charge recombination in FeTPPCl-PCN composite is significantly reduced. The improved charge separation and transfer in the FeTPPCl-PCN composite is further confirmed by the electrochemical impedance spectra (EIS) measurement. Generally, charge transfer resistance in the photocatalysts could be evaluated from the arc radius of the resultant EIS Nyquist plots. As widely reported, the large arc radius represents weak charge separation in semiconducting nanomaterials.[29] As clear from Figure 4c, the FeTPPCl-PCN composite reveals a small arc radius of the EIS Nyquist plot in

comparison to that of the PCN and FeTPPCl photocatalysts, signifying the remarkably improved charge separation and transfer.

Further, electron paramagnetic resonance (EPR) spectra of PCN, FeTPPCl and FeTPPCl-PCN photocatalysts were measured as shown in Figure 4d. Based on this technique, the unpaired electrons in semiconductors give rise to the EPR signals usually located at g ≈ 2.002. Notably, the intensity of EPR signal is directly proportional to the number of unpaired electrons.[40] Interestingly, the PCN, FeTPPCl and FeTPPCl-PCN photocatalysts reveal a Lorentzian line with a g value of 2.002. Compared to that of the PCN and FeTPPCl, the EPR signal intensity of FeTPPCl-PCN photocatalyst is remarkably enhanced, revealing a significant increase in the number of unpaired electrons. This confirms the improved charge separation and transfer in the FeTPPCl-PCN composite. The photoelectrochemical (PEC) *I-t* curves of the PCN, FeTPPCl and FeTPPCl-PCN photocatalysts were measured in 1 M KOH electrolyte to further validate the enhanced charge carrier's separation in the FeTPPCl-PCN composite. As revealed in Figure 4e, the photocurrent response of the FeTPPCl-PCN photocatalyst is remarkably improved as compared to the bare PCN and FeTPPCl photocatalysts, further validating the significantly promoted charge carrier's separation and transfer. To further investigate the promoted lifetime of charge carriers in the FeTPPCl-PCN photocatalyst, time-resolved fluorescence decay spectra were measured (λ_{ex} = 375 nm) as revealed in the Supporting Information, Figure S4. The non-radiative-($\tau1$) and radiative-($\tau2$) processes primarily denote the decay time of the faster and slower components.[28] It is widely accepted that $\tau2$ originates from the indirect self-trapped excitons initiated via the trapped electrons, while, the $\tau1$ originates from the directly induced free electrons and holes. As obvious, the predicted $\tau1$ and $\tau2$ values for PCN photocatalyst are 2.17 (Rel% = 66.99) and 17.97 (Rel% = 33.01) nanoseconds (ns). Whereas, the predicted $\tau1$ and $\tau2$ values for FeTPPCl-PCN photocatalyst are 2.26 (Rel% = 65.50) and 19.56 (Rel% = 34.50) ns. The average lifetimes (τ_{avg}) PCN and FeTPPCl-PCN photocatalysts are 1.11 and 1.14 ns, respectively. This clearly demonstrates that the charge carrier's separation lifetime of the FeTPPCl-PCN photocatalyst is prolonged compared to that of the PCN photocatalyst. This well support the SPV, PL, EIS, EPR, and *I-t* curves results.

3.3. Photocatalytic Activities Evaluation. The photocatalytic water reduction tests for H_2 evolution under visible light and UV–visible illuminations were performed in an online gas reactor connected to the Gas Chromatography (TCD/FID). In the photocatalytic water reduction experiments, methanol was used as a sacrificial agent for capturing holes. As clear from Figure 4f, the PCN, FeTPPCl and FeTPPCl-PCN photocatalysts yield 103.48, 17.48, and 253.36 μmolg^{-1} of H_2, respectively, under visible illumination for 4 h. The rate of H_2 evolution over the FeTPPCl-PCN composite under visible light irradiation is □2.45-fold improved in comparison to that of the pristine PCN. Likewise, as revealed in Figure 4g, the PCN, FeTPPCl and FeTPPCl-PCN photocatalysts yield 1749.16, 67.7, and 8301 μmolg^{-1} of H_2, respectively, under UV-visible illumination for 4 h. The H_2 yield over the FeTPPCl-PCN composite is 4.75-fold improved compared to that of the bare PCN photocatalyst under UV-visible illumination. The H_2 production tests over the PCN and FeTPPCl-PCN photocatalysts were performed under single excitation wavelengths of 365 and 420 nm as revealed in Figure 4h. It is important to note that the photon with a wavelength of 365 nm exhibits high energy than the photon with a wavelength of 420 nm. Thus, a high amount of H_2 would be produced at wavelength 365 nm in comparison to that at 420 nm. As expected, the H_2 produced over PCN and FeTPPCl-PCN photocatalysts at 365 nm wavelength was 8.9 and 13.6 μmol, respectively. Likewise, the H_2 evolved over the PCN and FeTPPCl-PCN photocatalysts at wavelength 420 nm was 5.6 and 8.7 μmol, respectively. The predicted quantum efficiencies for H_2 evolution over the FeTPPCl-PCN photocatalyst at 365 and 420 nm wavelengths were 4.81 and 2.68%, respectively. As revealed in the Supporting Information Table S3, the predicted quantum efficiencies of our photocatalyst are remarkably higher than those of the previously reported CN based photocatalysts under identical conditions. Meanwhile, the photocatalytic recyclable tests for H_2 production over the FeTPPCl-PCN photocatalyst under visible and UV-visible illumination were measured as revealed in the Supporting Information Figure S5a and Figure 4i. As obvious, no significant decrease in the H_2 evolution activity can be observed even after four repeated photocatalytic cycles, confirming the excellent stability of the FeTPPCl-PCN photocatalyst.

Interestingly, this exceptional amount of H_2 produced over the PCN photocatalyst guarantee that the chemically exfoliated porous g-C_3N_4 exhibit a large surface area and abundant active sites for photocatalytic reaction. On the other hand, the superior H_2 evolution over the FeTPPCl-PCN composite is accredited to the abundant active sites due to the large surface area and the significantly promoted charge carrier's separation and transfer via the well-aligned type-II band heterostructure.

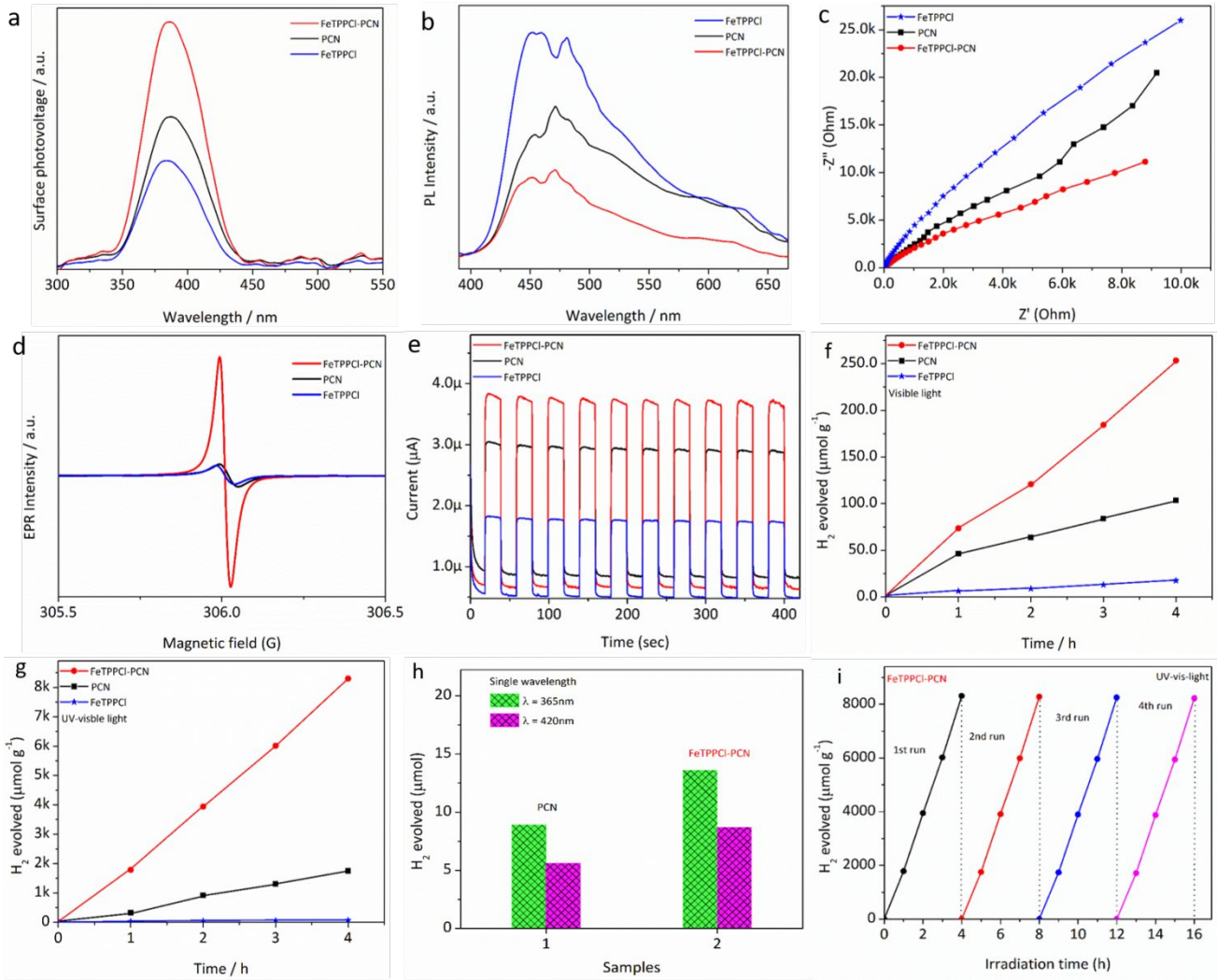

Figure 4 (a) SPV spectra (b) PL spectra, (c) EIS Nyquist plots, (d) EPR spectra, and (e) photoelectrochemical *I-t* curves of the PCN, FeTPPCl, and FeTPPCl-PCN photocatalysts. (f) Photocatalytic H_2 evolution activities of PCN, FeTPPCl, and FeTPPCl-PCN photocatalysts under visible light, and (g) under UV-visible light. (h) Photocatalytic H_2 evolution activities of PCN and FeTPPCl-PCN photocatalysts under single wavelengths (i.e., 365 and 420 nm) irradiation. (i) Photocatalytic recyclable test for H_2 evolution over the FeTPPCl-PCN photocatalyst under UV-vis light.

To validate the exceptional photocatalytic performance and high stability of the FeTPPCl-PCN composite, we have evaluated the electrochemical hydrogen evolution reaction (HER) of the PCN and FeTPPCl-PCN photocatalysts. The cyclic voltammetry (CV) curves for HER are revealed in the Supporting Information, Figure S5b. The CV curves were measured in 1 M KOH electrolyte vs. the Ag/AgCl electrode with scan rates of 50 mV sec^{-1}. Worth noting, the redox current of the FeTPPCl-PCN photocatalyst is remarkably improved signifying excellent electrochemical HER performance. Further, the FeTPPCl-PCN photocatalyst revealed more integrated areas in the CV curves compared to that of the PCN photocatalyst, confirming the remarkably enhanced specific capacity. According to the Randles–Sevcik equation,[46] the electro-active surface areas (ECSA) are directly proportional to the cathodic and anodic peaks. This means that the larger ECSA provides abundant active sites for electrochemical reactions. Thus, the improved photocatalytic and electrochemical performance of the FeTPPCl-PCN photocatalyst is accredited to the improved surface-active sites as well as the enhanced charge carrier's transfer and separation.

3.4. Ab-Initio Electronic Structure Property Simulations. Periodic density functional theory (DFT) simulations are performed on Quantum-ATK and the visualizations are attained on VNL 2019.12.[47] In order to model our experimentally fabricated catalyst, first we built the individual models of PCN and FeTPPCl, followed by a composite, and constructed two different types models (A and B), to represent composites of FeTPPCl-PCN. In model **A**, Cl atom of FeTPPCl directly interacts with PCN, which has less than 0.02 lattice mismatch as shown in Figure 5. While in the case of model **B**, Cl atom is situated at the interface of FeTPPCl-PCN catalyst as shown in the Supporting Information Figure S6c. Based on the excellent water interaction with the surface of FeTPPCl-PCN, we confirmed that model **A** is the correct model for our experimentally observed catalyst (*vide infra*). All these model structures were optimized at generalized-gradient approximation (GGA) via the Perdew Burke Ernzerh (PBE) of exchange correlation-functional and PseudoDojo

pseudopotential.[48,49] In this work, the linear combination of atomic orbitals (LCAO) technique is employed for Fe, Cl, C, N, O, and H atoms. A 5x5x1 Monkhorst-Packed k-grid and cut-off energy of 120 Hartree is utilized for the individual PCN, FeTPPCl, and FeTPCCL-PCN composite. Besides, the electron difference density (EDD), electron localization function (ELF), effective potential, and water interaction over the surface of FeTPPCl-PCN are also simulated with the above method.

In the final model structure of FeTPPCl-PCN (Figure 5c), the PCN and FeTPPCl have strong interactions with binding energy of -1.51 eV. This high interaction energy confirms the stability and feasibility of our photocatalyst. Moreover, the electrostatic potential map of FeTPPCl-PCN further validates and confirms the stability and activity of our photocatalyst as revealed in Figure 5d-f. From the electrostatic potential maps, we can see that the PCN (Figure 5d) and FeTPPCl (Figure 5e) photocatalysts have mutually shared their electronic cloud densities in FeTPPCl-PCN (see Figure 5f).

The results of model **B** are given in the Supporting Information Figure S7a-f. In addition, we have also simulated the ELF (Figure 5g-I, and Supporting Information Figure S7a-c) and EDD (Figure 6a, and Supporting Information Figure S7d) of these three photocatalysts. Before performing the HER mechanistic study of the FeTPPCl-PCN composite, a single water molecule was interacted over the surfaces of both model **A** and **B** (FeTPPCl-PCN@H_2O) and the system was allowed to be fully optimized. The optimized structures of FeTPPCl-PCN@H_2O for model **A** is given in Figure 6b, while model **B** is shown in the Supporting Information Figure S7e, where the H_2O interaction energy (ΔE_{int}) was calculated from the difference in energies of the optimized H_2O molecule and bare slab (E_{slab}) from the optimized H_2O-slab complex (*slab*@)H_2O, using equation (1).

$$\Delta E_{Int} = E_{slab@H2O} - (E_{H2O} + E_{slab}) \qquad (1)$$

The strong interaction energy of -11.85 kcal/mol of model **A** (-3.23 kcal/mol for model **B**) suggests the excellent HER performance of FeTPPCl-PCN as can be visualized from the ELF maps (see Figure 6c) and Table S1 and Table S2.

Based on this high interaction energy, model of FeTPPCl-PCN has been selected as a true representative of our experimentally observed photocatalyst. In Figure 6d, we can see that charge is transferred from PCN to FeTPPCl via Cl atom, which consequently makes the FeTPPCl photocatalyst more electroactive. So, water can be easily attracted by the surface of FeTPPCl-PCN due to its strong electron-donating nature. Actually, the O atom of water molecule interacted with the surface of FeTPPCl-PCN (see Supporting Information, Figure S8a, b). After optimization, O atom of H_2O formed strong electrostatic bonding with Fe of FeTPPCL-PCN (Figure 6b). While in the case of model **B**, where Cl is situated at the interface, and H atom of H_2O forms a hydrogen bonding with the surface atoms of FeTPPCl-PCN (see Supporting Information, Figure S9a, b).

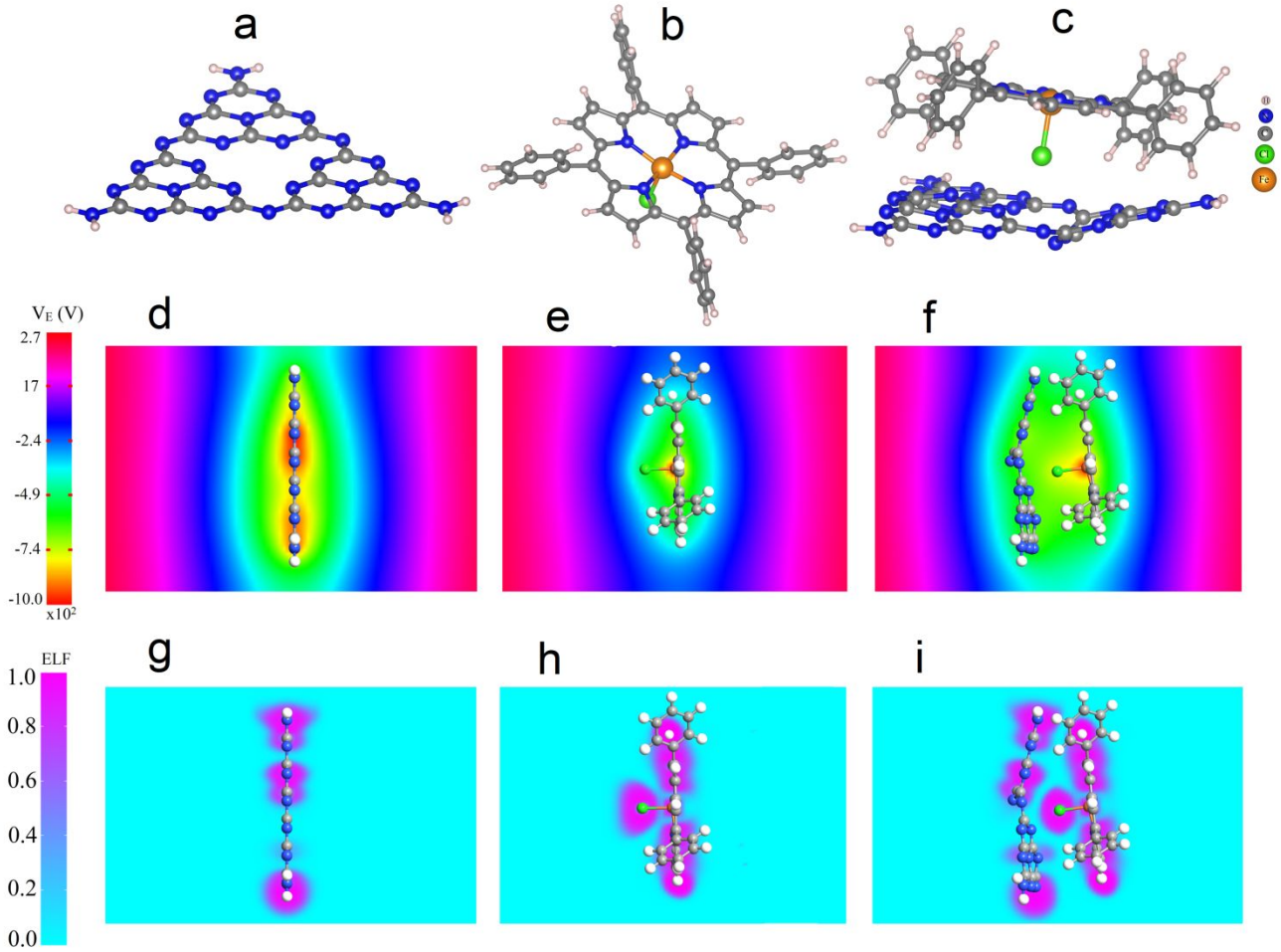

Figure 5. (a) Optimised geometric structure of PCN, (b) FeTPPCl, (c) and FeTPPCl-PCN (d), Electrostatic potential map of PCN, (e) FeTPPCl, (f) and FeTPPCl-PCN. Electron localization function maps (g) of PCN, (h) FeTPPCl , (i) and FeTPPCl-PCN.

The 2D EDD plots of pristine and water-interacted FeTPPCl-PCN systems are comparatively shown in Figure 6d, where the strong electron donating ability of the FeTPPCl-PCN photocatalyst is highlighted in a green dotted circle area, while the electron withdrawing part is denoted by blue-dotted circles. To further support the above results, the work functions of PCN, FeTPPCl, and FeTPPCl-PCN systems are simulated which are 6.51, 4.98, and 6.15 eV, respectively (see Figure 6e). The optimal work function of FeTPPCl-PCN is responsible for the excitation of an electron from the VB to the CB, making it available for photocatalytic reaction. This can consequently improve the electronegativity of FeTPPCl in the FeTPPCl-PCN composite. So, a catalyst with a lower work function is more active, as it can facilitate reactions with less energy input. This is due to the electrons in the valence band being more easily excited, making them more readily available for chemical reactions. So, a more electronegative FeTPPCl-PCN can easily reduce water and perform the HER process.

To determine the Gibbs free energies (ΔGH^*) of hydrogen adsorption, we choose model **A** of FeTPPCl-PCN. DFT calculations were performed to simulate the ΔGH^* adsorption on FeTPPCl-PCN as revealed in Figure 6f. The calculated ΔGH^* values at three different positions over the surface of FeTPPCl-PCN are marked as positions 1–3 and plotted in Figure 6f. In the case of position (i), H is adsorbed near Fe atom of the FeTPPCl-PCN, while in the case of position (ii), H is placed near N of the FeTPPCl-PCN. In the case of position (iii), H is placed between C and N of the FeTPPCl-PCN. All these positons are schematically shown in Figure 6g. The ΔGH^* values at positions 1–3 is 0.15, −0.62, and −0.71 eV, respectively.

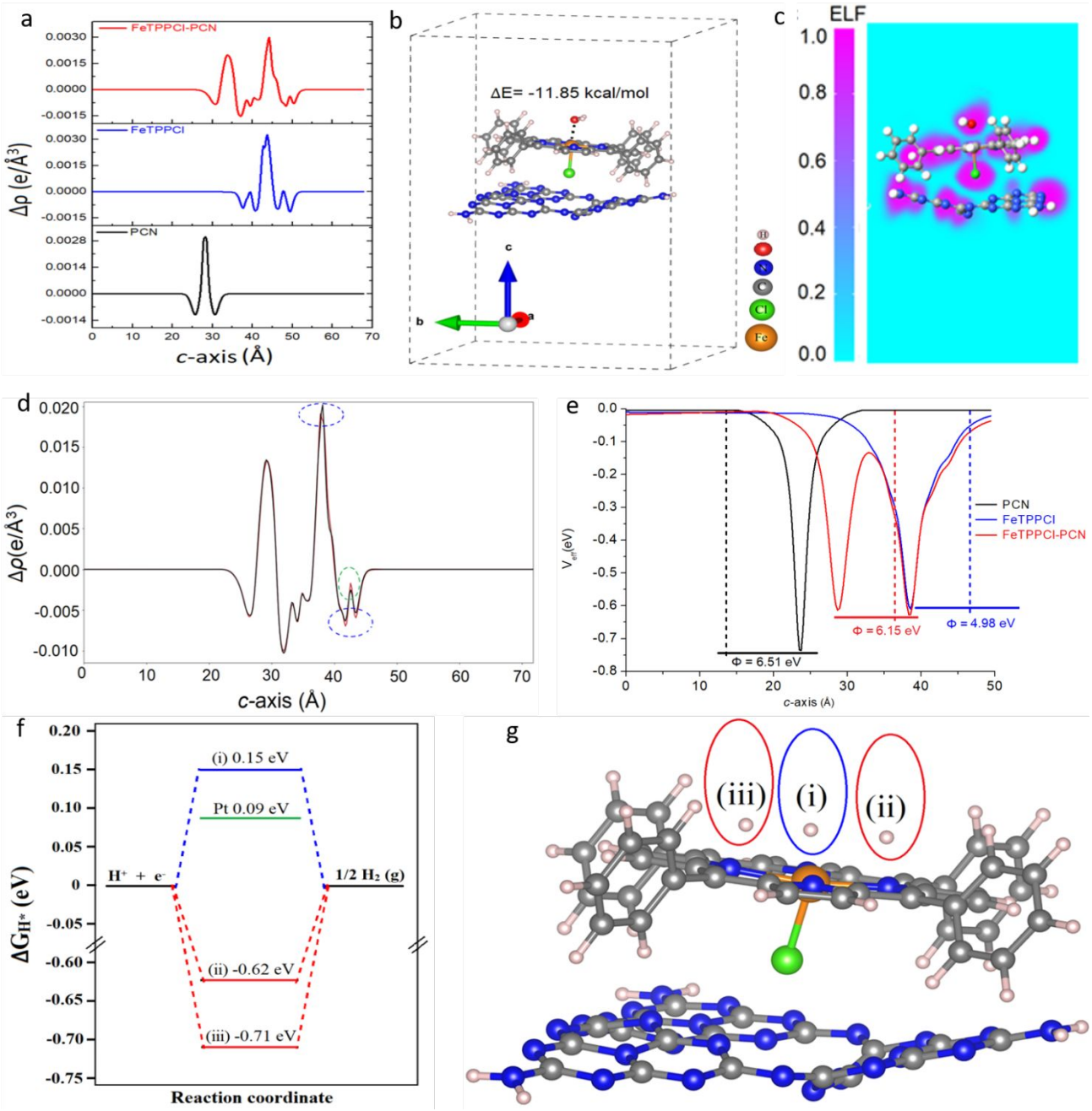

Figure 6. (a) EDD plots of PCN, FeTPPCl, and FeTPPCl-PCN. (b) Optimized geometric strucutre of FeTPPCl-PCN@H_2O type **A** system. c) Electron localization function map of FeTPPCl-PCN@H_2O, (d) the comparative EDD plots of FeTPPCl-PCN and FeTPPCl-PCN@H_2O. (e) Simulated effective potential maps of PCN, FeTPPCl, and FeTPPCl-PCN along with their work functions. (f) Gibbs free energy (ΔGH*) of HER process over the surface of FeTPPCl-PCN at three different positions along with Pt. (g) Schematic illustration for H adsorption at three different positions of FeTPPCl-PCN.

Based on a comparative analysis of Figure 6f, we predicted that the ΔGH* value at position (i) is optimal (i.e., 0.15 eV), responsible for the dissociation reaction, and exhibits increased catalytic activity. This could be due to electrostatic interaction between H and the Fe atom of FeTPPCl-PCN. The ΔGH* value at position number (ii) is greatest (i.e., −0.62 eV), which is owing to the strong adsorption energy (bonding) of the H atom with the N-atom over the catalyst's surface. This increased adsorption energy does not dissociate the hydrogen bonds, reducing the overall catalytic activity.

Moreover, the ΔGH* value at position (iii) is also very high (-0.71 eV) and again, here the H is also attached to N of FeTPPCl-PCN. In the case of both positions (ii) and (iii), H form a strong bonding with N of FeTPPCl-PCN. So, these higher ΔGH* values of H adsorption do not allow dissociation reaction. On the other hand, the ΔGH* value at position (i) has high activity for the HER, which is close to the thermodynamic limit value of 0. This value is also near to that of the Pt (111) surface, which is ~0.09 eV. The reason behind this is the charge transformation from PCN to FeTPPCl-PCN via Cl atoms, which optimize the charge of Fe. It is found that the FeTPPCl-PCN is a promising

candidate for highly efficient HER. Furthermore, we suggest that the enhanced HER activity of FeTPPCl-PCN is due to the porous support of PCN, which has enhanced photocatalytic activities of the surface where H is adsorbed (see Figure 6g).

3.5. Discussion on Mechanism. It is important to mention that charge carriers' separation and transfer is the crucial step in semiconductor photocatalysis. In the case of composite photocatalysts, the transfer of electrons mainly relies on the appropriate band structure alignment. As predicted from the Tauc plots, the energy band gaps of PCN, and FeTPPCl-PCN photocatalysts are 2.77 and 2.96 eV, respectively. The corresponding valence band edges of PCN, and FeTPPCl-PCN are 1.76 and 2.08 V, respectively, versus the NHE as predicted from the valence band XPS measurement. The conduction band potential values of the PCN and FeTPPCl-PCN photocatalysts can be predicted from the band gap equation (i.e., $E_{CB} = E_{VB} - E_{Eg}$) as mentioned in the previous reports.[50,51] Herein, we have predicted the values of E_g and E_{VB} for both of the PCN and FeTPPCl-PCN photocatalysts. Hence, their exact E_{CB} values are predicted to be −1.01 and −0.88 V, respectively. According to the predicted valence and conduction band edge values of the PCN and FeTPPCl-PCN catalysts, a type-II charge transfer mechanism is possible in the FeTPPCl-PCN composite as predicted in Scheme 1. Based on the above elucidation, it is assumed that when the heterostructure FeTPPCl-PCN photocatalyst is excited under visible or UV-visible irradiation, charge carriers are generated in both of the components (i.e., carbon nitride and porphyrin). Since the conduction band edge of PCN photocatalyst is more negative than that of the FeTPPCl photocatalyst, the excited electrons of PCN will easily transfer to the conduction band of FeTPPCl photocatalyst. More important, the valence band edge of the FeTPPCl photocatalyst is more positive than that of the PCN photocatalyst. Thus, the photoinduced holes of FeTPPCl photocatalyst will transfer to the valence band of PCN photocatalyst. As a result of the type-II band alignment in the FeTPPCl-PCN composite, lifetime of the photoinduced charge carriers significantly improved, and as a result, the H_2 evolution activity is remarkably enhanced. In summary, the newly designed FeTPPCl-PCN composite revealed high performance for water reduction to evolve H_2, which is due to the large specific surface area, abundant active sites, and significantly enhanced charge carrier's separation and transfer.

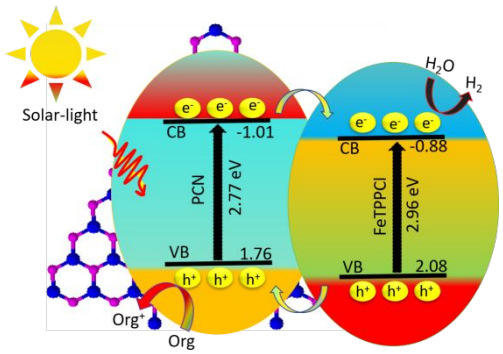

Scheme 1. Schematic of the band alignment, charge carriers transfer, and the photocatalytic reactions over the surface of FeTPPCl-PCN composite.

4. CONCLUSIONS

In summary, we have successfully fabricated porous g-C_3N_4 (PCN) via sulfuric acid-assisted chemical exfoliation method and then coupled it with Iron(III) meso-tetraphenylporphine chloride (FeTPPCl) porphyrin via the wet-chemical method. The FeTPPCl-PCN composite revealed exceptional performance for H_2 evolution with a quantum yield of 4.81 and 2.68% at single excitation wavelengths of 365 and 420 nm, respectively. From experimental results, it is confirmed that the enhanced performance for H_2 evolution is accredited to the improved surface-active sites due to porous structure and the significantly improved charge carrier's separation via the well-aligned type-II band heterostructure. Our density functional theory (DFT) simulations strongly validate the excellent HER performance of FeTPPCl-PCN in the form of optimum ΔGH* value of 0.15 eV which is near to Pt (0.09 eV) catalyst. It is inferred that the combination of PCN and FeTPPCl led to a stable photocatalyst due to the strong electrostatic interaction (-1.51 eV) in them, resulting in a decreased local work function on the surface of FeTPPCl-PCN, which consequently enhanced the HER activity. We suggest that the resultant composite would be a perfect model for the design and fabrication of high-efficiency heterostructure photocatalysts for energy applications.

ASSOCIATED CONTENT

Supporting Information

(Supplementary material include Images of the chemical exfoliation of bulk CN to PCN, SEM images, TEM, BET, XPS spectra, Time-resolved fluorescence decay spectra, H_2 evolution stability test under visible light, cyclic voltammogram curves, Electron localization function maps, Tables for simulated total energy and interaction energy of the catalysts, model structure of water interacted FeTPPCl-PCN before and after optimization, theoretical methodology for gibbs free energy of H, comparative table for the quantum efficiency yield for H_2 evolution and quantum efficiency calculation).

The Supporting Information is available free of charge on the ACS Publications website.

AUTHOR INFORMATION

Corresponding Authors

Wei Luo – *School of Optical and Electronic Information, Wuhan National Laboratory for Optoelectronics, Engineering Research Center for Functional Ceramics of the Ministry of Education, Huazhong University of Science and Technology, Wuhan 430074, People's Republic of China*
luowei@mail.hust.edu.cn

Chundong Wang – *School of Optical and Electronic Information, Wuhan National Laboratory for Optoelectronics, Engineering Research Center for Functional Ceramics of the Ministry of Education, Huazhong University of Science and Technology, Wuhan 430074, People's Republic of China*
apcdwang@hust.edu.cn

Authors

Muhammad Humayun – *School of Optical and Electronic Information, Wuhan National Laboratory for Optoelectronics, Engineering Research Center for Functional Ceramics of the Ministry of Education, Huazhong University of Science and Technology, Wuhan 430074, People's Republic of China*

Habib Ullah – *Department of Renewable Energy, Faculty of Environment, Science and Economy, University of Exeter, Penryn Campus, Cornwall TR10 9FE, United Kingdom*

Chao Hu – *School of Chemical Engineering and Pharmacy, Wuhan Institute of Technology, Wuhan, 430073, China*

Mi Tian – *Department of Engineering, Faculty of Environment, Science and Economy, University of Exeter, EX4 4QF, United Kingdom*

Wenbo Pi – *School of Optical and Electronic Information, Wuhan National Laboratory for Optoelectronics, Engineering Research Center for Functional Ceramics of the Ministry of Education, Huazhong University of Science and Technology, Wuhan 430074, People's Republic of China*

Yi Zhang – *School of Chemical Engineering and Pharmacy, Wuhan Institute of Technology, Wuhan, 430073, China*

Author Contributions

The manuscript was written by Muhammad Humayun with contributions of all authors. All authors have given approval to the final version of the manuscript. CRediT: **Muhammad Humayun** conceptualization, data curation, formal analysis, investigation, methodology, project administration, resources, validation, writing-original draft, writing-review & editing; **Habib Ullah** data curation, investigation, methodology, validation, DFT analysis, writing-review & editing; **Chao Hu** data curation, formal analysis; **Mi Tian** data curation, investigation, methodology, validation, DFT analysis, writing-review & editing; **Wenbo Pi** data curation, formal analysis; **Yi Zhang** conceptualization, investigation, methodology, project administration, resources; investigation; **Wei Luo** investigation, project administration, resources, supervision, writing-review & editing; **Chundong Wang** funding acquisition, project administration, resources, supervision, writing-review & editing.

Funding Sources

The work was financially supported by the Ministry of Science and Technology of China (Grant No. 2018YFA0702100), the National Natural Science Foundation of China (Grant No. 11874169, 51972129), and the National Key R&D Program of China (Grant No. 2017YFE0120500), Bintuan Science and Technology Program (Grants No. 2020DB002, 2022DB009), the Key Research and Development Program of Hubei (Grant No. 2020BAB079), and Ministry of Science and Technology Foreign Youth Talent Program Funding (Grant No. QN2022154003L).

Notes

The authors declare no competing financial interest.

ACKNOWLEDGMENT

We thank Dr. Habib Ullah and Dr. Mi Tian for their help in DFT simulations and valuable comments and suggestions and the authors of the University of Exeter's Advanced Research Computing facilities (Athena HPC Cluster) for carrying out this work and the Interreg 2 Seas program 2014–2020 co-funded by the European Regional Development Fund under subsidy contract no. 2S03-019, for the provision of QuantumATK_2019.12 software.

REFERENCES

(1) Verma, P.; Singh, A.; Rahimi, F. A.; Sarkar, P.; Nath, S.; Pati, S. K.; Maji, T. K. Charge-Transfer Regulated Visible Light Driven Photocatalytic H_2 Production and CO_2 Reduction in Tetrathiafulvalene Based Coordination Polymer Gel. *Nat. Commun.* **2021,** *12* (1), 7313.

(2) Zhang, Y.; Zhao, J.; Wang, H.; Xiao, B.; Zhang, W.; Zhao, X.; Lv, T.; Thangamuthu, M.; Zhang, J.; Guo, Y.; Ma, J.; Lin, L.; Tang, J. W.; Huang, R.; Liu, Q. J. Single-Atom Cu Anchored Catalysts for Photocatalytic Renewable H_2 Production with a Quantum Efficiency of 56%. *Nat. Commun.* **2022,** *13* (1), 58.

(3) Chen, Z.; Chen, P.; Xing, P.; Hu, X.; Lin, H.; Wu, Y.; Zhao, L.; He, Y. Novel Carbon Modified $KTa_{0.75}Nb_{0.25}O_3$ Nanocubes with Excellent Efficiency in Photocatalytic H_2 Evolution. *Fuel* **2018,** *233*, 486.

(4) Marwat, M. A.; Humayun, M.; Afridi, M. W.; Zhang, H.; Abdul Karim, M. R.; Ashtar, M.; Usman, M.; Waqar, S.; Ullah, H.; Wang, C. D.; Wei, L. Advanced Catalysts for Photoelectrochemical Water Splitting. *ACS Appl. Energy Mater.* **2021,** *4* (11), 12007.

(5) Humayun, M.; Wang, C.; Luo, W. Recent Progress in the Synthesis and Applications of Composite Photocatalysts: A Critical Review. *Small Methods* **2022,** *6* (2), 2101395.

(6) Lu, Y.; Yin, W.-J.; Peng, K.-L.; Wang, K.; Hu, Q.; Selloni, A.; Chen, F.-R.; Liu, L.-M.; Sui, M.-L. Self-Hydrogenated Shell Promoting Photocatalytic H_2 Evolution on Anatase TiO_2. *Nat. Commun.* **2018,** *9* (1), 2752.

(7) Humayun, M.; Shu, L.; Pi, W.; Xia, H.; Khan, A.; Zheng, Z.; Fu, Q.; Tian, Y.; Luo, W. Vertically Grown CeO_2 and TiO_2 Nanoparticles Over the MIL53Fe MOF as Proper Band Alignments for Efficient H_2 Generation and 2,4-DCP Degradation. *Environ. Sci. Poll. Res.* **2022,** *29* (23), 34861.

(8) Humayun, M.; Raziq, F.; Khan, A.; Luo, W. Modification Strategies of TiO_2 for Potential Applications in Photocatalysis: A Critical Review. *Green Chem. Lett. Rev.* **2018,** *11* (2), 86.

(9) Luo, N.; Montini, T.; Zhang, J.; Fornasiero, P.; Fonda, E.; Hou, T.; Nie, W.; Lu, J.; Liu, J.; Heggen, M.; Lin,

L.; Ma, C. T.; Wang, M.; Fan, F.T.; Jin, S.; Wang, F. Visible-Light-Driven Coproduction of Diesel Precursors and Hydrogen from Lignocellulose-Derived Methylfurans. *Nat. Energy* **2019,** *4* (7), 575.

(10) Humayun, M.; Ullah, H.; Usman, M.; Habibi-Yangjeh, A.; Tahir, A. A.; Wang, C.; Luo, W. Perovskite-Type Lanthanum Ferrite Based Photocatalysts: Preparation, Properties, and Applications. *J. Energy Chem.* **2022,** *66*, 314.

(11) Bozal-Ginesta, C.; Rao, R. R.; Mesa, C. A.; Liu, X.; Hillman, S. A. J.; Stephens, I. E. L.; Durrant, J. R. Redox-State Kinetics in Water-Oxidation IrO_x Electrocatalysts Measured by Operando Spectroelectrochemistry. *ACS Catal.* **2021,** *11* (24), 15013.

(12) Nishiyama, H.; Yamada, T.; Nakabayashi, M.; Maehara, Y.; Yamaguchi, M.; Kuromiya, Y.; Nagatsuma, Y.; Tokudome, H.; Akiyama, S.; Watanabe, T.; Narushima, R.; Okunaka, S.; Shibata, N.; Takata, T.; Hisatomi T.; Domen K. Photocatalytic Solar Hydrogen Production from Water on a 100-m^2 Scale. *Nature* **2021,** *598* (7880), 304.

(13) Li, X.; Zhao, L.; Yu, J.; Liu, X.; Zhang, X.; Liu, H.; Zhou, W. Water Splitting: From Electrode to Green Energy System. *Nano-Micro Lett.* **2020,** *12* (1), 131.

(14) Usman, M.; Zeb, Z.; Ullah, H.; Suliman, M. H.; Humayun, M.; Ullah, L.; Shah, S. N. A.; Ahmed, U.; Saeed, M. A review of Metal-Organic Frameworks/Graphitic Carbon Nitride Composites for Solar-Diven Green H_2 Production, CO_2 Reduction, and Water Purification. *J. Environ. Chem. Eng.* **2022,** *10* (3), 107548.

(15) Zhu, J.; Xiao, P.; Li, H.; Carabineiro, S. A. C. Graphitic Carbon Nitride: Synthesis, Properties, and Applications in Catalysis. *ACS Appl. Mater. Interfaces* **2014,** *6* (19), 16449.

(16) Humayun, M.; Ullah, H.; Tahir, A. A.; bin Mohd Yusoff, A. R.; Mat Teridi, M. A.; Nazeeruddin, M. K.; Luo, W. An Overview of the Recent Progress in Polymeric Carbon Nitride Based Photocatalysis. *The Chem. Rec.* **2021,** *21* (7), 1811.

(17) Zhang, Q.; Chen, P.; Chen, L.; Wu, M.; Dai, X.; Xing, P.; Lin, H.; Zhao, L.; He, Y. Facile Fabrication of Novel Ag_2S/K-g-C_3N_4 Composite and its Enhanced Performance in Photocatalytic H_2 Evolution. *J. Colloid Interface Sci.* **2020,** *568*, 117.

(18) Chen, P.; Xing, P.; Chen, Z.; Hu, X.; Lin, H.; Zhao, L.; He, Y. In-Situ Synthesis of $AgNbO_3$/g-C_3N_4 Photocatalyst via Microwave Heating Method for Efficiently Photocatalytic H_2 Generation. *J. Colloid Interface Sci.* **2019,** *534*, 163.

(19) Chen, P.; Chen, L.; Ge, S.; Zhang, W.; Wu, M.; Xing, P.; Rotamond, T. B.; Lin, H.; Wu, Y.; He, Y. Microwave Heating Preparation of Phosphorus Doped g-C_3N_4 and its Enhanced Performance for Photocatalytic H_2 Evolution in the Help of Ag_3PO_4 Nanoparticles. *Int. J. Hydrog. Energy* **2020,** *45* (28), 14354.

(20) Wang, Q.; Fang, Z.; Zhao, X.; Dong, C.; Li, Y.; Guo, C.; Liu, Q.; Song, F.; Zhang, W. Biotemplated g-C_3N_4/Au Periodic Hierarchical Structures for the Enhancement of Photocatalytic CO_2 Reduction with Localized Surface Plasmon Resonance. *ACS Appl. Mater. Interfaces* **2021,** *13* (50), 59855.

(21) Zhang, X.; Chen, S.; Lian, X.; Dong, S.; Li, H.; Xu, K. Efficient Activation of Peroxydisulfate by g-C_3N_4/Bi_2MoO_6 Nanocomposite for Enhanced Organic Pollutants Degradation through Non-Radical Dominated Oxidation Processes. *J. colloid interface sci.* **2022,** *607*, 684.

(22) Ong, W. J.; Tan, L. L.; Ng, Y. H.; Yong, S. T.; Chai, S. P. Graphitic Carbon Nitride (g-C_3N_4)-Based Photocatalysts for Artificial Photosynthesis and Environmental Remediation: Are We a Step Closer to Achieving Sustainability? *Chem. Rev.* **2016,** *116* (12), 7159.

(23) Papailias, I.; Todorova, N.; Giannakopoulou, T.; Ioannidis, N.; Boukos, N.; Athanasekou, C. P.; Dimotikali, D.; Trapalis, C. Chemical vs Thermal Exfoliation of g-C_3N_4 for NO_x Removal Under Visible Light Irradiation. *Appl. Catal. B: Environ.* **2018,** *239*, 16.

(24) Tong, J.; Zhang, L.; Li, F.; Wang, K.; Han, L.; Cao, S. Rapid and High-Yield Production of g-C_3N_4 Nanosheets via Chemical Exfoliation for Photocatalytic H_2 Evolution. *RSC Adv.* **2015,** *5* (107), 88149.

(25) Xu, J.; Gao, Q.; Wang, Z.; Zhu, Y. An All-Organic 0D/2D Supramolecular Porphyrin/g-C_3N_4 Heterojunction Assembled via π-π Interaction for Efficient Visible Photocatalytic Oxidation. *Appl. Catal. B: Environ.* **2021,** *291*, 120059.

(26) Zhang, X.; Lin, L.; Qu, D.; Yang, J.; Weng, Y.; Wang, Z.; Sun, Z.; Chen, Y.; He, T. Boosting Visible-Light Driven Solar-Fuel Production Over g-C_3N_4/Tetra(4-carboxyphenyl)porphyrin Iron(III) Chloride Hybrid Photocatalyst via Incorporation with Carbon Dots. *Appl. Catal. B: Environ.* **2020,** *265*, 118595.

(27) Chen, D.; Wang, K.; Hong, W.; Zong, R.; Yao, W.; Zhu, Y. Visible Light Photoactivity Enhancement via CuTCPP Hybridized g-C_3N_4 Nanocomposite. *Appl. Catal. B: Environ.* **2015,** *166-167*, 366.

(28) Humayun, M.; Ullah, H.; Cheng, Z.-E.; Tahir, A. A.; Luo, W.; Wang, C. Au Surface Plasmon Resonance Promoted Charge Transfer in Z-Scheme System Enables Exceptional Photocatalytic Hydrogen Evolution. *Appl. Catal. B: Environ.* **2022,** *310*, 121322.

(29) Humayun, M.; Ullah, H.; Shu, L.; Ao, X.; Tahir, A. A.; Wang, C.; Luo, W. Plasmon Assisted Highly Efficient Visible Light Catalytic CO_2 Reduction Over the Noble Metal Decorated Sr-Incorporated g-C_3N_4. *Nano-Micro Lett.* **2021,** *13* (1), 209.

(30) Rury, A. S.; Sension, R. J. Broadband Ultrafast Transient Absorption of Iron (III) Tetraphenylporphyrin Chloride in the Condensed Phase. *Chem. Phys.* **2013,** *422*, 220.

(31) Longevial, J.-F.; Clément, S.; Wytko, J. A.; Ruppert, R.; Weiss, J.; Richeter, S. Peripherally Metalated Porphyrins with Applications in Catalysis, Molecular

Electronics and Biomedicine. *Chem. Eur. J.* **2018,** *24* (58), 15442.

(32) Silvestri, S.; Fajardo, A. R.; Iglesias, B. A. Supported Porphyrins for the Photocatalytic Degradation of Organic Contaminants in Water: A Review. *Environ. Chem. Lett.* **2022,** *20* (1), 731.

(33) Bayon, A.; de la Calle, A.; Ghose, K. K.; Page, A.; McNaughton, R. Experimental, Computational and Thermodynamic Studies in Perovskites Metal Oxides for Thermochemical Fuel Production: A Review. *Int. J. Hydrog. Energy* **2020,** *45* (23), 12653.

(34) Wang, J.; Wang, Y.; Wang, W.; Ding, Z.; Geng, R.; Li, P.; Pan, D.; Liang, J.; Qin, H.; Fan, Q. Tunable Mesoporous g-C_3N_4 Nanosheets as a Metal-Free Catalyst for Enhanced Visible-Light-Driven Photocatalytic Reduction of U(VI). *Chem. Eng. J.* **2020,** *383*, 123193.

(35) Akple, M. S.; Low, J.; Wageh, S.; Al-Ghamdi, A. A.; Yu, J.; Zhang, J. Enhanced Visible Light Photocatalytic H_2-Production of g-C_3N_4/WS_2 Composite Heterostructures. *Appl. Surf. Sci.* **2015,** *358*, 196.

(36) Wang, Q.; Zhang, L.; Guo, Y.; Shen, M.; Wang, M.; Li, B.; Shi, J. Multifunctional 2D Porous g-C_3N_4 Nanosheets Hybridized with 3D Hierarchical TiO_2 Microflowers for Selective Dye Adsorption, Antibiotic Degradation and CO_2 Reduction. *Chem. Eng. J.* **2020,** *396*, 125347.

(37) Humayun, M.; Pi, W.; Yuan, Y.; Shu, L.; Cao, J.; Khan, A.; Zheng, Z.; Fu, Q.; Tian, Y.; Luo, W. A Rational Design of g-C_3N_4-Based Ternary Composite for Highly Efficient H_2 Generation and 2,4-DCP Degradation. *J. Colloid Interface Sci.* **2021,** *599*, 484.

(38) Humayun, M.; Hu, Z.; Khan, A.; Cheng, W.; Yuan, Y.; Zheng, Z.; Fu, Q.; Luo, W. Highly Efficient Degradation of 2,4-Dichlorophenol Over CeO_2/g-C_3N_4 Composites Under Visible-Light Irradiation: Detailed Reaction Pathway and Mechanism. *J. Hazard. Mater.* **2019,** *364*, 635.

(39) Lipińska, M. E.; Rebelo, S. L. H.; Freire, C. Iron(III) Porphyrin Anchored onto Organosilylated Multiwalled Carbon Nanotubes as an Active Catalyst for Epoxidation Reactions under Mild Conditions. *J. Mater. Sci.* **2014,** *49* (4), 1494.

(40) Zou, W.; Liu, X.-H.; Xue, C.; Zhou, X.-T.; Yu, H.-Y.; Fan, P.; Ji, H.-B. Enhancement of the Visible-Light Absorption and Charge Mobility in a Zinc Porphyrin Polymer/g-C_3N_4 Heterojunction for Promoting the Oxidative Coupling of Amines. *Appl. Catal. B: Environ.* **2021,** *285*, 119863.

(41) Ma, T.; Shen, Q.; Xue, B. Z. J.; Guan, R.; Liu, X.; Jia, H.; Xu, B. Facile Synthesis of Fe-doped g-C_3N_4 for Enhanced Visible-Light Photocatalytic Activity. *Inorg. Chem. Commun.* **2019,** *107*, 107451.

(42) Sun, Y.; Qi, X.; Li, R.; Xie, Y.; Tang, Q.; Ren, B. Hydrothermal Synthesis of 2D/2D BiOCl/g-C_3N_4 Z-Scheme: For TC Degradation and Antimicrobial Activity Evaluation. *Optic. Mater.* **2020,** *108*, 110170.

(43) Humayun, M.; Zada, A.; Li, Z.; Xie, M.; Zhang, X.; Qu, Y.; Raziq, F.; Jing, L. Enhanced Visible-Light Activities of Porous $BiFeO_3$ by Coupling with Nanocrystalline TiO_2 and Mechanism. *Appl. Catal. B: Environ.* **2016,** *180*, 219.

(44) Humayun, M.; Sun, N.; Raziq, F.; Zhang, X.; Yan, R.; Li, Z.; Qu, Y.; Jing, L. Synthesis of ZnO/Bi-doped Porous $LaFeO_3$ Nanocomposites as Highly Efficient Nano-photocatalysts Dependent on the Enhanced Utilization of Visible-Light-Excited Electrons. *Appl. Catal. B: Environ.* **2018,** *231*, 23.

(45) Ali, S.; Humayun, M.; Pi, W.; Yuan, Y.; Wang, M.; Khan, A.; Yue, P.; Shu, L.; Zheng, Z.; Fu, Q.; Wei, L. Fabrication of $BiFeO_3$-g-C_3N_4-WO_3 Z-Scheme Heterojunction as Highly Efficient Visible-Light Photocatalyst for Water Reduction and 2,4-Dichlorophenol Degradation: Insight Mechanism. *J. Hazard. Mater.* **2020,** *397*, 122708.

(46) Zheng, H.; Sun, X.; Liu, Y.; Jiang, S.; Wang, D.; Fan, Y.; Hu, L.; Zhang, D.; Yao, W.; Zhang, L. New g-C_3N_4/GO/MoS_2 Composites as Efficient Photocatalyst for Photocathodic Protection of 304 Stainless Steel. *Water Sci. Technol.* **2021,** *84* (3), 499.

(47) Smidstrup, S.; Markussen, T.; Vancraeyveld, P.; Wellendorff, J.; Schneider, J.; Gunst, T.; Verstichel, B.; Stradi, D.; Khomyakov, P. A.; Vej-Hansen, U. G.; Lee, M. E.; Chill, S. T.; Rasmussen, F.; Penazzi, G.; Corsetti, F.; Ojanperä, A.; Jensen, K.; Palsgaard, M. L. N.; Martinez, U.; Blom, A.; Brandbyge, M.; Stokbro, K. QuantumATK: An Integrated Platform of Electronic and Atomic-Scale Modelling Tools. *J. Phys. Condens. Matter* **2019,** *32* (1), 015901.

(48) Enkovaara, J.; Rostgaard, C.; Mortensen, J. J.; Chen, J.; Dułak, M.; Ferrighi, L.; Gavnholt, J.; Glinsvad, C.; Haikola, V.; Hansen, H. A.; Kristoffersen, H. H.; Kuisma, M.; Larsen, A. H.; Lehtovaara, L.; Ljungberg, M.; Lopez-Acevedo, O.; Moses, P. G.; Ojanen, J.; Olsen, T.; Petzold, V.; Romero, N. A.; Stausholm-Møller, J.; Strange, M.; Tritsaris, G. A.; Vanin, M.; Walter, M.; Hammer, B.; Häkkinen, H.; Madsen, G. K. H.; Nieminen, R. M.; Nørskov, J. K.; Puska, M.; Rantala, T. T.; Schiøtz, J.; Thygesen, K. S.; Jacobsen, K. W. Electronic Structure Calculations with GPAW: a Real-Space Implementation of the Projector Augmented-Wave Method. *J. phys. Condens Matter* **2010,** *22* (25), 253202.

(49) van Setten, M. J.; Giantomassi, M.; Bousquet, E.; Verstraete, M. J.; Hamann, D. R.; Gonze, X.; Rignanese, G. M. The PseudoDojo: Training and Grading a 85 Element Optimized Norm-Conserving Pseudopotential Table. *Comput. Phys. Commun.* **2018,** *226*, 39.

(50) Wang, Y.; Tan, G.; Liu, T.; Su, Y.; Ren, H.; Zhang, X.; Xia, A.; Lv, L.; Liu, Y. Photocatalytic Properties of the g-C_3N_4/{010} Facets $BiVO_4$ Interface Z-Scheme Photocatalysts Induced by $BiVO_4$ Surface Heterojunction. *Appl. Catal. B: Environ.* **2018,** *234*, 37.

(51) Yosefi, L.; Haghighi, M. Fabrication of Nanostructured Flowerlike p-BiOI/p-NiO Heterostructure and its Efficient Photocatalytic

Performance in Water Treatment Under Visible-Light Irradiation. *Appl. Catal. B: Environ.* **2018,** *220*, 367.

TOC Graphic